WELDING INSPECTION USING NOVEL SPECULARITY FEATURES AND A ONE-CLASS SVM

Fabian Timm, Sascha Klement, Thomas Martinetz and Erhardt Barth
Institute for Neuro- and Bioinformatics, University of Luebeck, Ratzeburger Allee 160, Luebeck, Germany

Keywords: Feature extraction, One-class classification, Welding seam inspection, Machine vision.

Abstract: We present a framework for automatic inspection of welding seams based on specular reflections. Therefore, we introduce a novel feature set – called specularity features (SPECs) – describing statistical properties of specular reflections. For classification we use a one-class support-vector approach. The SPECs significantly outperform statistical geometric features and raw pixel intensities, since they capture more complex characteristics and depencies of shape and geometry. We obtain an error rate of 9%, which corresponds to the level of human performance.

1 INTRODUCTION

In many industrial processes individual parts are joined by using welding techniques. Soldering and welding techniques are common in diverse areas such as printed circuit board assembly or automotive line spot welding. The quality of a single welding often defines the grade of the whole product, for example in critical areas such as automotive or aviation industry, where failures of the welding process can cause a malfunction of the whole product. Typically, welds are made by a laser or a soldering iron. During the last few years lasers and their usage in industrial applications have become affordable for many companies. Although the initial cost of a laser-welding system is still high, their wearout is low and so the service intervals are very long. A laser weld is more precise than a weld by a soldering iron, but the quality can also vary due to shifts of the part towards the laser or due to material impurities. Therefore, an inspection of the welding is required in order to guarantee an accurate quality.

There are several machine vision approaches to automatically classify the quality of solder joints. These approaches can be divided into two groups. The first group deals with special camera and lighting setups to gain the best image representation of the relevant features (Ong et al., 2008; Kim and Cho, 1995; Chiu and Perng, 2007). In the second group, the camera and lighting setup is often predetermined and the inspection is done by sophisticated pattern recognition methods. In the last few years several approaches for automatic inspection of solder joints concerning feature extraction, feature selection, and classification were proposed (Ko and Cho, 2000; Poechmueller et al., 1991; Ong et al., 2008; Driels and Lee, 1988; Kim and Cho, 1995). Like in many other applications, neural networks and especially the support-vector-machine have become state-of-the-art (Cortes and Vapnik, 1995; Boser et al., 1992; Vapnik, 1995).

In this work we focus on the inspection of cathodes welded by an Nd:YAG (neodymium-doped yttrium aluminium garnet) laser during the production of lamps. Due to its position in the whole production process, the camera and lighting setup was fixed and could not be changed. Since the welded cathode has specific specular reflections, an appropriate feature extraction is required in order to achieve an accurate performance. Therefore, we introduce a novel feature set called specularity features (SPECs). The SPECs contain statistics of certain shape characteristics of single components and can cover a wide range of complex shape properties and their dependencies. For the classification we use a one-class support-vector approach (Schölkopf et al., 2001; Tax and Duin, 2004; Labusch et al., 2008) in order to describe features of accurate weldings and to separate them from all other possible inaccurate weldings. We also evaluate those SPECs that are most relevant for the classification and compare them to the physical shape of the cathode.

For comparison we use raw pixel intensities and the statistical geometric feature (SGF) algorithm which computes simple geometric characteristics of binary components.

Timm F., Klement S., Barth E. and Martinetz T.
WELDING INSPECTION USING NOVEL SPECULARITY FEATURES AND A ONE-CLASS SVM.
DOI: 10.5220/0001776301450152
In *Proceedings of the Fourth International Conference on Computer Vision Theory and Applications (VISIGRAPP 2009)*, page
ISBN: 978-989-8111-69-2

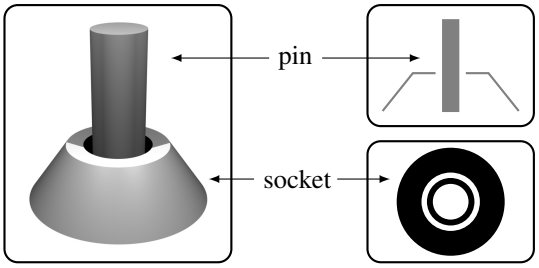

Figure 1: A 3d drawing of the cathode (left), a cross-section (upper right) and the image of the camera are shown (lower right).

In section 2 we give a brief overview of the camera and lighting setting and the image acquisition. The methods for feature extraction and classification are described in section 3. Experiments and the results are shown in section 4. We conclude with a discussion in section 5.

2 IMAGE ACQUISITION

An unwelded cathode consists of a socket and a pole that may be composed of different materials (see Fig. 1). In a top view with directional parallel light the unwelded cathode simplifies to only four components – two black rings (the slant of the neck and the space between pin and socket), one white ring (neck of the socket) and one white circle (top of the pin, see Fig. 1 bottom right). Hence, a component analysis of the grey value image of the welded cathode can be used to extract specific features.

A correct combination of camera, lens and illumination is very important to achieve the best performance in classification. However, sometimes the best setup can not be chosen due to limited space or other requirements. For this work, there was only one camera setup practicable (see Fig. 2). We used a standard analog monochrome VGA video camera, a single-sided telecentric lens and a LED ring light with a Fresnel lens. We collected 934 images containing 657 images of non-defective cathodes and 277 images of defective cathodes. All images were labelled by experts, scaled to unit size (96×96 pixel) and smoothed by a Gaussian filter (5×5, $\sigma = 1$). The unwelded cathodes are first separated by a simple template matching such that the dataset contains images of welded cathodes. Moreover, the dataset only consists of images which are difficult to classify manually.

Since defective cathodes are determined by the mean time to failure, the true class labels are not known in general. Therefore, the experts look for aberrations that were selected by extensive benchmark tests. Example images of defective and non-defective cathodes are shown in Fig. 3. The reflections of cathodes without a defect vary due to differences in material and position of the pin. Also, a slight deflection of the pin just before the welding can affect the quality of the welding. Some of the defective cathodes have holes caused by a slanted pin, others do not have any reflections due to a very rough surface. Therefore, the variety of defects can not be described easily, and a feature extraction method that covers several geometric properties and complex dependencies between components is required.

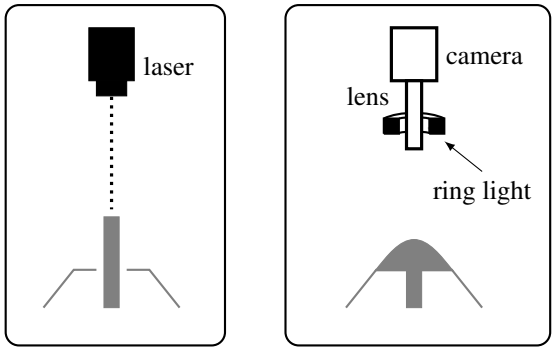

Figure 2: Drawing of the setup for laser welding (left) and image acquisition (right). The laser and the camera are located on top of the cathode. The distance between the LED ring light and the cathode is chosen such that angle of incidence is very small.

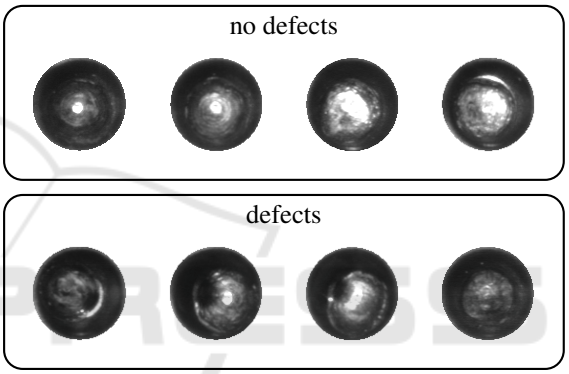

Figure 3: Example images of cathodes (top row) and defective cathodes (bottom row).

3 METHODS

Recently, several approaches for the inspection of solder joints were proposed (Ong et al., 2008; Chiu and Perng, 2007; Ko and Cho, 2000; Kim and Cho, 1995; Driels and Lee, 1988). Some of these methods compute simple features in a manually tiled binary image, others use the pixel intensities directly as input fea-

tures for a neural network or a support vector machine (Cortes and Vapnik, 1995; Boser et al., 1992; Vapnik, 1995). Hence, the preprocessing often involves a considerable downsampling of the images in order to reduce the dimensionality. Usually, this downsampling reduces the information of the images and yields poor error rates. A better performance is achieved by extracting specific features that describe the relevant reflections of the weldings.

In this work, we present a novel approach for the extraction of specularity features called SPECs. These features describe several complex properties of specular reflections and their dependencies. For comparison we also use the statistical geometric feature (SGF) approach as well as raw pixel intensities.

In the following, we will describe the extraction of SGFs and SPECs. Since the images were recorded by an 8bit monochrome camera, we focus on grey value images, but the approach can easily be extended to colour images.

3.1 Statistical Geometric Features

Originally, SGFs were used for texture classification with 16 features for each image (Chen et al., 1995). Further extensions were developed for cell nuclei classification and contained 48 features (Walker and Jackway, 1996). SGFs compute simple shape properties of local components. Hence, they can be used to extract specific features of welding images. Moreover, SGFs are very intuitive and computed efficiently.

For each l-bit grey value image I a stack of binary images $\mathcal{B} = \{I_\tau\}$ with $\tau \in \{1,2,3,...,2^l\}$ is generated. A single binary image I_τ is computed such that

$$I_\tau(x,y) = \begin{cases} 1 & : \quad I(x,y) \geq \tau \\ 0 & : \quad I(x,y) < \tau \end{cases} \quad . \tag{1}$$

This decomposition is lossless, since the input image can always be recovered by summing up all binary images. Furthermore, each binary image I_τ is decomposed into a set of black and white components, $\{\mathbf{C}_0(\tau), \mathbf{C}_1(\tau)\}$ with $\mathbf{C}_0(\tau) = \{C_{(0,\tau)_1}, ..., C_{(0,\tau)_m}\}$, and $\mathbf{C}_1(\tau) = \{C_{(1,\tau)_1}, ..., C_{(1,\tau)_n}\}$, respectively (see Fig. 4). The subscript 0 denotes a black component and the subscript 1 a white component.

Each component $C_{(j,\tau)_i} = \{\vec{x}_k\}$ consists of pixel positions $\vec{x}_k \in \{1,2,...,H\} \times \{1,2,...,W\}$, where H and W are the height and the width of the input image. For convenience we omit the indices of a component if they are not necessary. We also use $C_i = C_{(j,\tau)_i}$ for abbreviation.

The area of a component equals the number of its pixels,

$$\texttt{AREA}(C) = \texttt{card}(C) \quad . \tag{2}$$

The relative size of a single component C_i with respect to all components is defined as

$$\texttt{PROP}(C_i) = \frac{\texttt{AREA}(C_i)}{\sum_k \texttt{AREA}(C_k)} \quad . \tag{3}$$

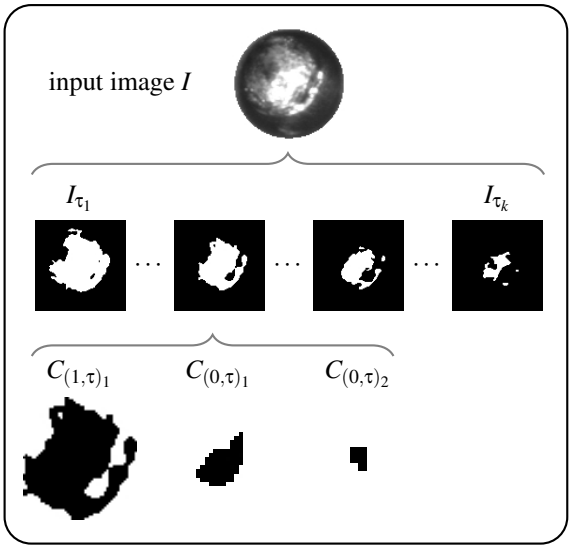

Figure 4: Decomposition scheme for a grey value input image. First, the input image (first row) is decomposed into several binary images I_τ (second row). Afterwards each binary image is further separated into its black and white components (third row). The white component $C_{(1,\tau)_1}$ is inverted, for convenience.

Based on the stack of binary images, the feature extraction of the SGF algorithm can be divided into two stages – a local stage and a global stage. In the local stage several features for each component are calculated (see Tab. 1). A single binary image is then described by a set of averaged shape and position properties of all black and white components.

In the second stage the local features are combined to global features using first order statistics (see Tab. 2). In total, the SGF algorithm determines 48 features for a single input image.

3.2 Specularity Features (SPEC)

Since the statistical geometric features were mainly developed for classification of textures, i.e. repetitive patterns, they are not suitable for the inspection of welding seams, which usually do not have a repetitive structure. Instead, properties that describe the characteristic shapes of specular reflections are required. For example, some defective cathodes have long narrow reflections at the neck of the socket which can

Table 1: Local features for a single binary image I_τ of size $H \times W$ (Walker and Jackway, 1996).

description	formula		
number of black/white components	$\mathtt{NOC}(\tau)$	$=$	$\lvert\mathbf{C}(\tau)\rvert$
averaged irregularity	$\overline{\mathtt{IRGL}}(\tau)$	$=$	$\frac{\sum_k \mathtt{IRGL}(C_k)\,\mathtt{AREA}(C_k)}{\sum_k \mathtt{AREA}(C_k)}$
averaged clump displacement	$\overline{\mathtt{DISP}}(\tau)$	$=$	$\frac{1}{\mathtt{NOC}(\tau)}\sum_k \mathtt{DISP}(C_k)$
averaged clump inertia	$\overline{\mathtt{INERTIA}}(\tau)$	$=$	$\frac{1}{\mathtt{NOC}(\tau)}\sum_k \mathtt{DISP}(C_k)\,\mathtt{AREA}(C_k)$
total clump area	$\mathtt{TAREA}(\tau)$	$=$	$\frac{1}{HW}\sum_k \mathtt{AREA}(C_k)$
averaged clump area	$\overline{\mathtt{CAREA}}_i(\tau)$	$=$	$\frac{1}{\mathtt{NOC}(\tau)}\sum_k \mathtt{AREA}(C_k)$

where

$\mathtt{IRGL}(C) = \dfrac{1+\sqrt{\pi}\,\max_{\vec{x}\in C}\,\|\vec{x}-\vec{\mu}(C)\|}{\sqrt{\mathtt{AREA}(C)}} - 1$ is the irregularity of the component C,

$\mathtt{DISP}(C) = \sqrt{\pi}\,\dfrac{\|\vec{\mu}(C)-\vec{\mu}_I\|}{\sqrt{HW}}$ is the relative displacement of the component C,

$\vec{\mu}(C)$ is the centre of gravity of the component C and $\vec{\mu}_I$ is the centre of the image.

be covered by features such as the formfactor and the extent.

We make use of the general decomposition scheme of binary images and evaluate appropriate features covering the properties of specular reflections. We compute several general properties of each component (see Tab. 3). Using a 4-neighbourhood two successive boundary points are denoted by $\vec{x}_m$ and $\vec{x}_{m+1}$, $F(\alpha)$ is the maximum distance between two boundary points when rotating the coordinate axis by $\alpha \in \mathcal{A} = \{0°, 5°, ..., 175°\}$, w_{BR} and h_{BR} are the width and height of the bounding rectangle and a, b are the major and minor axis of the ellipse that has the same second moments as the region. For a detailed discussion on geometric shapes see chapter 9 of (Russ, 2007).

Table 2: Global features. f is one of the local features described before.

`maximum`	$= \max_\tau f(\tau)$
`mean`	$= \dfrac{1}{\lvert\tau\rvert}\sum_\tau f(\tau)$
`sample mean`	$= \dfrac{1}{\sum_\tau f(\tau)}\sum_\tau \tau f(\tau)$
`sample std.`	$= \sqrt{\dfrac{\sum_\tau (\tau - \mathtt{sample\ mean})^2 f(\tau)}{\sum_\tau f(\tau)}}$

The local features are computed for each component and need to be combined to form a single feature. Hence, we scale each feature in two different ways. First, we calculate the mean weighted by the relative size of the components, and second, we scale the sum by the total number of components. For example, for the averaged perimeter of the binary image I_τ these two scalings are:

$$\overline{\mathtt{PERIM}}(\tau) = \sum_k \mathtt{PERIM}(C_k)\,\mathtt{PROP}(C_k) \ , \quad (4)$$

$$\overline{\mathtt{PERIM}}(\tau) = \frac{1}{\mathtt{NOC}(\tau)}\sum_k \mathtt{PERIM}(C_k) \ , \quad (5)$$

where $\mathtt{PROP}(C_k)$ is defined in Eq. 3. Using these scalings two aspects can be covered simultaneously. On the one hand, if small reflections are important, they are considered by scaling with the number of components. On the other hand, if large reflections are relevant, they become important when scaling by the relative size.

We combine the local features by computing `minimum`, `variance`, `median`, and `entropy` besides the statistics of Tab. 2. Whereas the `sample mean` and `sample std.` range over the threshold τ, the new features are statistics over local shape features. Hence, we can, for example, evaluate the variance of the number of white components or the entropy of the formfactor of white components. Moreover, extreme shape properties of components become less important when using the `median`.

In total, for a single image, we determine 768 features consisting of:

Table 3: Features for a component C.

perimeter:

$$\texttt{PERIM}(C) = \sum_{m=1}^{N-1} \|\vec{x}_m - \vec{x}_{m+1}\|_2$$

maximum Feret diameter:

$$\texttt{MAXFD}(C) = \max_{\alpha\in\mathcal{A}} F(\alpha)$$

minimum Feret diameter:

$$\texttt{MINFD}(C) = \min_{\alpha\in\mathcal{A}} F(\alpha)$$

mean Feret diameter:

$$\texttt{MEANF}(C) = \frac{1}{|\mathcal{A}|}\sum_{\alpha\in\mathcal{A}} F(\alpha)$$

variance Feret diameter:

$$\texttt{VARFD}(C) = \frac{1}{|\mathcal{A}|}\sum_{\alpha\in\mathcal{A}} \left[F(\alpha) - \texttt{MEANF}(C)\right]^2$$

area of bounding rectangle:

$$\texttt{AREAB}(C) = w_{\texttt{BR}}\, h_{\texttt{BR}}$$

eccentricity:

$$\texttt{ECCEN}(C) = \frac{\sqrt{a^2+b^2}}{a}$$

aspect ratio:

$$\texttt{ASPRA}(C) = \frac{\texttt{MAXFD}(\tau)}{\texttt{MINFD}(\tau)}$$

extent:

$$\texttt{EXTEN}(C) = \frac{\texttt{AREA}(C)}{\texttt{AREAB}(C)}$$

formfactor:

$$\texttt{FORMF}(C) = \frac{4\,\pi\,\texttt{AREA}(C)}{\texttt{PERIM}(C)^2}$$

roundness:

$$\texttt{ROUND}(C) = \frac{4\,\texttt{AREA}(C)}{\pi\,\texttt{MAXFD}(C)^2}$$

compactness:

$$\texttt{COMPT}(C) = \frac{2\sqrt{\texttt{AREA}(C)}}{\sqrt{\pi}\;\texttt{MAXFD}(C)}$$

regularity of aspect ratio:

$$\texttt{REGAR}(C) = \left[1 + \texttt{VARFD}(C) + \texttt{MAXFD}(C) - \texttt{MINFD}(C)\right]^{-1}$$

- 48 local features for a single component (24 for a black component and 24 for a white component),
- 2 scaling methods (by the proportional size and by the total number of components), and
- 8 global statistics.

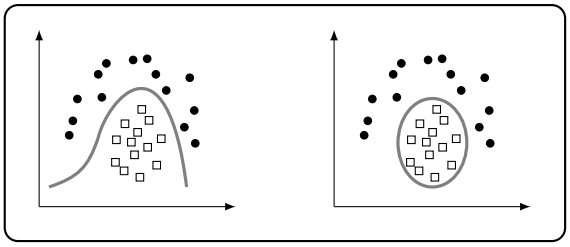

Figure 5: Comparison of a two-class SVM (left) and a one-class SVM (right). The positive class is depicted by white squares, the negative class (outlier) is shown by black circles and the class boundary (separating hyperplane) is shown in gray.

3.3 Classification

The support vector machine (SVM) has become a very useful approach for classification and yields best performances on several benchmark datasets (Cortes and Vapnik, 1995; Boser et al., 1992; Vapnik, 1995). Standard two-class SVMs require samples that describe *both* classes in a proper way. In our case, however, there are only a few defective cathodes that are characterised well. We therefore apply a one-class support-vector machine. Furthermore, we make use of a simple incremental training algorithm with several improvements for fast parameter validation (Labusch et al., 2008; Timm et al., 2008; Tax and Duin, 2004; Schölkopf et al., 2001). In contrast to standard two-class SVMs, which separate the input space into two half-spaces, one-class SVMs learn a subspace such as to enclose the samples of only the target class (see Fig. 5). This increases the robustness against unknown classes of outliers and also extends the time intervals for retraining when new samples are available.

4 EXPERIMENTS AND RESULTS

In the following, different sets of features are compared and analysed with respect to their separation capabilities. These feature sets are:

- raw pixel intensities of scaled images (12 × 12 pxl → 144 features),
- raw pixel intensities of scaled images (24 × 24 pxl → 576 features),
- SGFs (48 features), and
- preselected SPECs (48 features).

Since the performance of the SGFs can vary depending on the grey level depth of the images we used different depths ranging from 2bit to 8bit (Walker

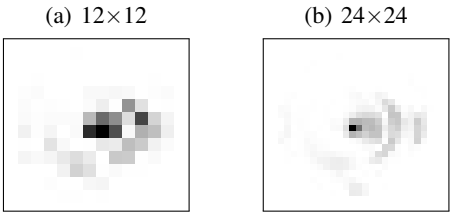

Figure 6: Relevant pixel positions in the image. Dark values indicate high relevance. Pixels in the image centre have large values and are therefore relevant. This confirms the description of non-defective weldings which have a white reflection at this position.

and Jackway, 1996) and two different sizes (12×12, 24×24). The raw pixel intensities are only used as a baseline. We selected the 48 most important features from the SPECs to evaluate the performance with the same number of features as the SGFs. The preselection of these 48 features was done by computing the discriminant value d of each feature i:

$$d(i) = 2\,\frac{(\mu_+(i)-\mu_-(i))^2}{\sigma_+^2(i)+\sigma_-^2(i)}\quad , \tag{6}$$

where $\mu_+(i)$, $\mu_-(i)$ are the means of the positive and negative class concerning feature i, and $\sigma_+^2(i)$, $\sigma_-^2(i)$ are the class specific variances (Fukunaga, 1972). The 48 features with the highest discriminant values are then chosen as input features for the one-class SVM. This very simple ranking method is not optimal in the sense that it identifies the best subset of features, but it is computationally efficient and yields good results.

For the SVM we chose a Gaussian kernel and evaluated the best parameters by 10-fold cross validation (Stone, 1974). To avoid numerical problems we scaled the input features to $[-1,+1]$. Each constant feature, e.g. the minimum over certain local features, was removed before training to speed up the algorithm and to save memory. For a comparison of the different feature extraction methods we applied a Wilcoxon signed rank test to the test errors.

Since no benchmark datasets of solder joint images are available, we only applied the feature extraction methods to images of laser-weldings.

4.1 Results of Feature Ranking

Relevant features of the raw pixel intensities are mostly located in the centre (see Fig. 6). This corresponds to the description in Sec. 2 where white reflections (regions) in the centre of the image indicate good weldings. The ring structure, i.e. the neck of the socket, can also be detected, which is relevant for defective weldings (see Fig. 6 (left), Fig. 1 (lower right)). Obviously, this depends neither on the size of the images nor on their quantisation.

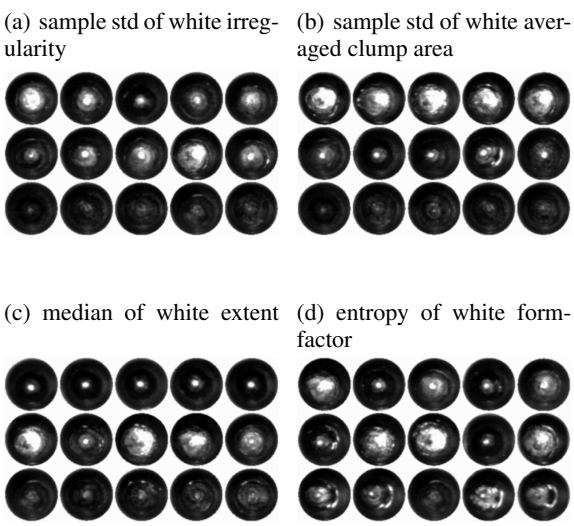

Figure 7: Example images with large values of the indicated features (top row), medium (middle row) and small (bottom row).

The most relevant features among the SGFs are:

- sample std. of white irregularity (see Fig. 7a),
- sample std. of white averaged clump area (see Fig. 7b),
- mean of white displacements,
- mean of white irregularity, and
- mean of number of white components.

Not only the positions of white components are important but also their size and irregularity. Compared to the raw pixel intensities the SGFs can also cover shape properties of local components (see Fig. 6, 7a, 7b).

The most relevant SPECs are:

- median of the white extent (scaled by the number of components (NOC), see Fig. 7c),
- median of the white compactness (scaled by NOC),
- median of the white minimum distance from the image centre (scaled by NOC),
- entropy of the white formfactor (scaled by NOC, see Fig. 7d), and
- mean of white eccentricity (scaled by NOC).

Compared to the SGFs, more complex features become significant, such as the extent or the form factor, which can describe, for example, small white reflections in the image centre and holes in the socket of defective cathodes simultaneously (seeFig. 7c, 7d).

Table 4: Frequency of the different local and global features for the 48 most relevant features when combining SGFs and SPECs.

name	occurrence
scale by number of comp.	37
scale by relative area	11
white properties	48
black properties	0
local SPECs	47
local SGFs	1
global SPECs	22
global SGFs	16

When combining SGFs and SPECs only one SGF is present in the 48 most relevant features which indicates the quality of the SPECs (see Tab. 4). Furthermore, scaling by the number of components is more important than scaling by their relative size. Hence, small white regions are also responsible for defective weldings, e.g. if they are located at the neck of the socket (see Fig. 7(d) bottom row). Altogether, the large number of extended shape properties (47) and new global statistics (16) shows that the SPEC features describe the relevant image properties of welded cathodes more accurately than the SGFs.

4.2 Results of Classification

The results for the different feature extraction methods applied to images of welded cathodes show several aspects.

First, features of images of higher grey level depth (6 – 8 bit) yield significantly lower error rates than features of lower depth (see Fig. 9). This is independent of the feature extraction method and confirms the complexity of specular reflections in terms of grey values.

Second, no significant difference between the two image sizes could be observed, i.e. grey level resolution is more important than spatial resolution (see Fig. 9, 8). If the image size is lower than 12×12, however, the higher relevance of the grey level depth compared to image size does not hold, since the structures of the welded pin and the socket are merged, e.g. holes and rings (see Fig. 3 bottom left) cannot be detected. Also, SGFs and SPECs of images with a higher grey value resolution perform significantly better (see Fig. 9b, c).

Third, the SPECs (6 bit) have the lowest error rate of 9.2% and perform significantly better than the SGFs (7 bit, error rate 11.5%, $p = 0.029$, see Fig. 8). Hence, SPECs describe the specular reflections of welded cathodes more precisely than SGFs and yield a more accurate classification.

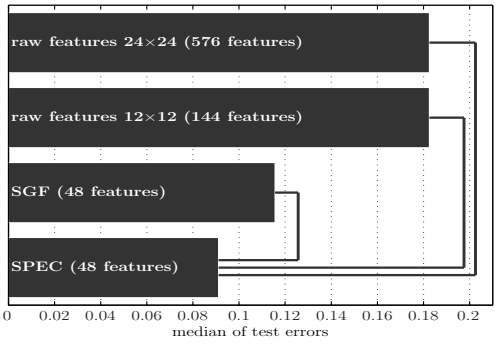

Figure 8: Comparison of the methods. Some of the significant differences ($p < 0.05$) are indicated by black lines.

Fourth, the SPECs (6 bit) significantly outperform the raw pixel intensities (error rate 18%, image depth of 7 bit, see Fig. 8). Hence, the raw pixel intensities can only cover very simple image properties, e.g. white reflections in the centre of the image, and they are not able to describe holes or dependencies between reflections accurately.

5 CONCLUSIONS

We introduced a novel set of specularity features (SPECs) for welding seam inspection and showed that these features significantly outperform the statistical geometric features as well as raw pixel intensities. We extracted the relevant features of the SPECs and found white regions in the centre of the image and their shape to be of high importance for the classification. The SPECs can cover several complex shape properties and their dependencies and are, nevertheless, intuitive and computed efficiently. Hence, they are well appropriate for the automatic inspection of welding seams and can even be applied to a wider range of machine vision problems concerning complex specular reflections, such as surface inspection or defect detection of specular objects.

The labelling of the datasets of solder joints or other weldings is usually based on experts viewing images and not on the actual functional test. Hence, these labels are very subjective and do not necessarily correspond to the physical and electrical properties of the weldings. Therefore, additional information about the welding, e.g. the conductivity, rigidity or weld strength, has to be collected and combined with a machine-vision based approach in order to improve the results.

The results may further be improved using other feature selection methods. However, the error rates

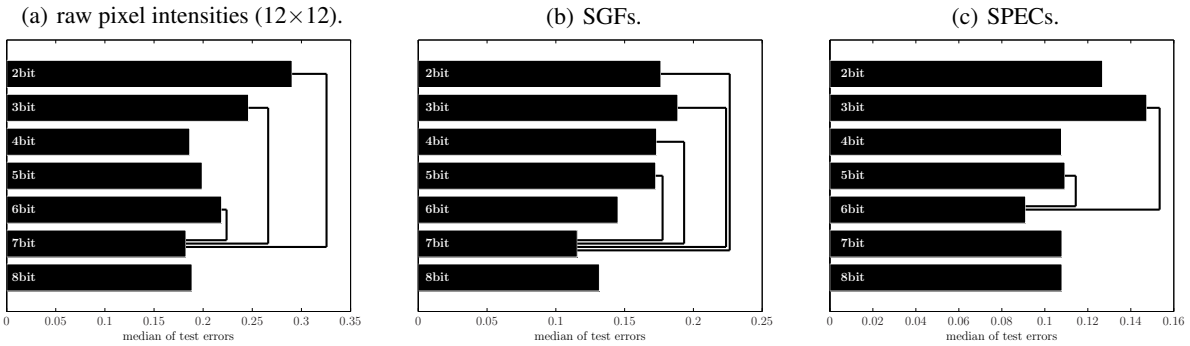

Figure 9: Medians of test errors. Black lines indicate a significant difference ($p < 0.05$) between two methods. Only significant differences of the best depth level to all others are considered in the plot.

of the novel SPEC features are comparable to those obtained by manual inspection.

REFERENCES

Boser, B., Guyon, I., and Vapnik, V. (1992). A training algorithm for optimal margin classifiers. In Haussler, D., editor, *Proc. of the 5th Annual ACM Workshop on Computational Learning Theory*, pages 144–152. ACM Press.

Chen, Y. Q., Nixon, M. S., and Thomas, D. W. (1995). Statistical geometrical features for texture classification. *Pattern Recognition*, 28(4):537–552.

Chiu, S. and Perng, M. (2007). Reflection-area-based feature descriptor for solder joint inspection. *Machine Vision and Applications*, 18(2):95–106.

Cortes, C. and Vapnik, V. (1995). Support-vector networks. *Machine Learning*, 20(3):273–297.

Driels, M. and Lee, C. (1988). Feature selection for automatic visual inspection of solder joints. *The Int. Journal of Advanced Manufacturing Technology*, 3:3–32.

Fukunaga, K. (1972). *Introduction to Statistical Pattern Recognition*. Academic Press.

Kim, J. and Cho, H. (1995). Neural network-based inspection of solder joints using a circular illumination. *Image and Vision Computing*, 13(6):479–490.

Ko, K. and Cho, H. (2000). Solder joints inspection using a neural network and fuzzy rule-based classification method. *IEEE Transactions on Electronics Packaging Manufacturing*, 23(2):93–103.

Labusch, K., Timm, F., and Martinetz, T. (2008). Simple incremental one-class support vector classification. In Rigoll, G., editor, *Proc. of the 30th German Pattern Recognition Symposium DAGM*, volume 5096 of *Lecture Notes in Computer Science*, pages 21–30. Springer.

Ong, T., Samad, Z., and Ratnam, M. (2008). Solder joint inspection with multi-angle imaging and an artificial neural network. *The Int. Journal of Advanced Manufacturing Technology*, 38(5–6):455–462.

Poechmueller, W., Glesner, M., Listl, L., and Mengel, P. (1991). Automatic classification of solder joint images. In *Proc. of the Int. Joint Conf. on Neural Networks*, volume 2, pages 933–940. IEEE Computer Society Press.

Russ, J. C. (2007). *The Image Processing Handbook*. CRC Press.

Schölkopf, B., Platt, J. C., Shawe-Taylor, J., Smola, A. J., and Williamson, R. C. (2001). Estimating the support of a high-dimensional distribution. *Neural Computation*, 13(7):1443–1471.

Stone, M. (1974). Cross-validatory choice and assessment of statistical predictions. *Journal of the Royal Statistics Society*, 36:111–147.

Tax, D. M. J. and Duin, R. P. W. (2004). Support vector data description. *Machine Learning*, 54(1):45–66.

Timm, F., Klement, S., and Martinetz, T. (2008). Fast model selection for maxminover-based training of support vector machines. In *Proc. of the 19th Int. Conf. on Pattern Recognition*, Florida, USA. IEEE Computer Society Press. to appear.

Vapnik, V. (1995). *The Nature of Statistical Learning Theory*. Springer Verlag, New York.

Walker, R. and Jackway, P. T. (1996). Statistical geometric features: Extensions for cytological texture analysis. In *Proc. of the 13th Int. Conf. on Pattern Recognition*, pages 790–794. IEEE Computer Society Press.